ELSEVIER

Journal of Fluids and Structures 26 (2010) 1018–1033

JOURNAL OF FLUIDS AND STRUCTURES

www.elsevier.com/locate/jfs

Fluid–structure coupling for an oscillating hydrofoil

C. Münch*, P. Ausoni, O. Braun, M. Farhat, F. Avellan

Laboratory for Hydraulic Machines, Ecole Polytechnique Fédérale de Lausanne, 33bis, av. de Cour, CH-1007 Lausanne, Switzerland

Received 11 August 2009; accepted 7 July 2010
Available online 21 August 2010

Abstract

Fluid-structure investigations in hydraulic machines using coupled simulations are particularly time-consuming. In this study, an alternative method is presented that linearizes the hydrodynamic load of a rigid, oscillating hydrofoil. The hydrofoil, which is surrounded by incompressible, turbulent flow, is modeled with forced and free pitching motions, where the mean incidence angle is 0° with a maximum angle amplitude of 2°. Unsteady simulations of the flow, performed with ANSYS CFX, are presented and validated with experiments which were carried out in the EPFL High-Speed Cavitation Tunnel. First, forced motion is investigated for reduced frequencies ranging from 0.02 to 100. The hydrodynamic load is modeled as a simple combination of inertia, damping and stiffness effects. As expected, the potential flow analysis showed the added moment of inertia is constant, while the fluid damping and the fluid stiffness coefficients depend on the reduced frequency of the oscillation motion. Behavioral patterns were observed and two cases were identified depending on if vortices did or did not develop in the hydrofoil wake. Using the coefficients identified in the forced motion case, the time history of the profile incidence is then predicted analytically for the free motion case and excellent agreement is found for the results from coupled fluid–structure simulations. The model is validated and may be extended to more complex cases, such as blade grids in hydraulic machinery.

Keywords: Fluid-structure interactions; Added mass; Fluid damping; Fluid stiffness; Oscillating hydrofoil; Hydraulic machines and system

1. Introduction

Fluid-structure interactions play a significant role in many engineering applications, particularly in hydraulic machinery. For instance, a rotor–stator interaction will induce pressure fluctuations, which can lead to vibrations of the guide vane or resonance in the distributor channels (Zobeiri et al., 2006; Nicolet et al., 2006). The flow-induced vibrations of the guide vane, excited by von Kármán vortex shedding (Ausoni et al., 2007), can also lead to premature cracks. Thus, there is strong interest to study the elastic behavior of vibrating blade grids to design safe and reliable turbines and pump-turbines (Wang et al., 2009; Gnesin et al., 2004).

Different methods that model fluid–structure coupling have been extensively investigated; see Dowell and Hall (2001) for a comprehensive review. Predictive methods for aero engines or gas turbines are divided into two classes depending on coupling strength (Marshall and Imregun, 1996): classical and integrated. The former combines the fluid and structural equations in an uncoupled way, whereas the latter solves the equations simultaneously.

*Corresponding author. Tel.: +41 21 693 36 43.
E-mail address: cecile.munch@epfl.ch (C. Münch).

0889-9746/$ - see front matter © 2010 Elsevier Ltd. All rights reserved.
doi:10.1016/j.jfluidstructs.2010.07.002

Integrated or partially integrated methods account for energy transfer by considering both the structural and aero-damping. An integrated method developed by Carstens et al. (2003) investigated the aero-elastic behavior of vibrating blades assemblies and analyzed the flutter behavior of turbomachinery bladings. Moffatt and He (2005) predicted the resonant forced response of turbomachinery blades using fully coupled methods and expected that, by combining the aerodynamic forcing and damping calculations into a single analysis, a higher computational efficiency would result compared with using a classical method. In that study, results for a NASA Rotor 67 transonic aero-fan rotor showed that coupled methods must use multiple solutions to find the resonant peak.

The classical method is the preferred approach to study blade row interaction problems due to its ability to accurately predict the resonant peak from a single solution. Young (2007, 2008) analyzed time-dependent hydroelastic phenomena in a ship propeller with cavitation using a classical method by developing a 3-D potential-based boundary element method coupled with a 3-D finite element method. With water as the surrounding fluid, the predicted performance curves, blade tip deflections, cavitation inception coefficient values, cavitation patterns and fundamental frequencies agreed well with experimental measurements and observations. Ducoin et al. (2009) numerically analyzed a deformable hydrofoil with transient pitching motion with a CFD finite volume code (CFX) for the fluid and a CSD finite element code (ANSYS) for the structure. A one-way approach was used, and there was good agreement with the experiments for the maximum displacement of the hydrofoil at low pitching velocity. However, for the highest pitching velocity, the simulation showed a stronger hysteresis effect than the experiment. This difference is attributed to the damping, which was not considered in the structure model.

Coupled simulations for complex geometries, like hydraulic machines, are extremely time consuming using either the classical or integrated method. Therefore, in this paper, a model is proposed that avoids that type of complex simulation for a rigid, oscillating hydrofoil. The unsteady incompressible and turbulent flow around a forced and free oscillating hydrofoil is numerically and experimentally investigated. The hydrodynamic load is modeled as a combination of inertial, damping and stiffness effects, where the primary focus is to determine the inertial effects. Brennen (1982) established formulae that estimated the added mass and added moment of inertia from the fluid for simple geometries. According to Conca et al. (1997), the added mass for a moving body immersed in an incompressible liquid does not depend on the viscosity or the surrounding flow. In other words, the added mass can be calculated as if the fluid is inviscid and at rest. However, fluid damping and fluid stiffness effects cannot be estimated with empirical formulae. Experiments and numerical simulations are required to identify those effects because they depend on both the surrounding flow and the motion of the structure. First, the forced motion case is investigated in the frequency domain to identify the three effects. The free motion case is then used to assess the model by comparing the incidence angle time history determined by the linearized model with coupled fluid–structure simulations.

Section 2 introduces the case study and describes the numerical and experimental set up. In Section 3, the results are presented. The numerical simulations are also validated; the grid and time-step independencies are checked, and good agreement was found between the predicted and experimental values for the hydrodynamic torque. The hydrodynamic load is then analyzed. The method to determine the added moment of inertia, the fluid damping and fluid stiffness coefficient is detailed and assessed. Finally concluding remarks are given.

2. Set-up

2.1. Case studies

The hydrofoil used in both the numerical and experimental cases is a rounded trailing edge NACA 0009 (Abbott et al., 1945) with a chord length of 100 mm and a maximum thickness of 9.27 mm, as seen in Fig. 1.

Two types of pitching motions are considered: forced and free oscillations. In both cases, the hydrofoil rotates around its center of mass with a mean incidence angle, α_c, of 0° and a maximum angle amplitude, α_0, of 2°.

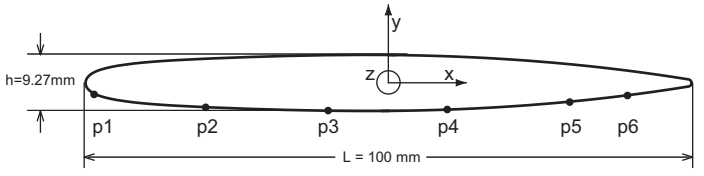

Fig. 1. NACA0009 Hydrofoil with rounded trailing edge.

For the forced motion case, as seen in Fig. 2, the instantaneous angle of attack, $\alpha(t)$, is defined by

$$\alpha(t) = \alpha_c + \alpha_0 \sin(\omega t), \tag{1}$$

where ω is the imposed angular pulsation. Table 1 summarizes the numerical and experimental conditions for forced motion, where the upstream velocity is C_{ref}, the reduced frequency is defined as $\kappa = \omega L/2C_{\mathrm{ref}}$ and the Reynolds number is defined as $\mathrm{Re} = C_{\mathrm{ref}} L/\nu$, where L is the hydrofoil chord length and ν is the kinematic viscosity of water.

For the free motion case, as seen in Fig. 3, the hydrofoil is attached to a flexible structure. The oscillating hydrofoil is a 1-degree-of-freedom model. The structural parameters of the hydrofoil are the moment of inertia J_s, the stiffness k_s and the damping coefficient μ_s. At the beginning of the simulation, the hydrofoil departs from rest at an incidence angle, α_0, without an initial velocity. A Fortran program was used in the flow solver to couple the structure motion with the flow. The incidence of the hydrofoil was computed as a function of the structural parameters, the hydrodynamic torque M and the hydrofoil incidence at previous time steps:

$$M^n = J_s \ddot{\alpha}^n + \mu_s \dot{\alpha}^n + k_s \alpha^n, \tag{2}$$

$$M^n = J_s \frac{\alpha^{n+1} - 2\alpha^n + \alpha^{n-1}}{\Delta t^2} + \mu_s \frac{\alpha^n - \alpha^{n-1}}{\Delta t} + k_s \alpha^n, \tag{3}$$

$$\alpha^{n+1} = \alpha^n \left(2 - \frac{\mu_s}{J_s}\Delta t - \frac{k_s}{J_s}\Delta t^2\right) + \alpha^{n-1}\left(\frac{\mu_s}{J_s}\Delta t - 1\right) + \frac{\Delta t^2}{J_s} M^n. \tag{4}$$

The free motion conditions for the numerical simulations are given in Table 2.

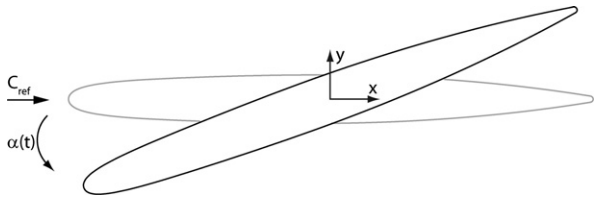

Fig. 2. Sketch of the forced oscillating case.

Table 1
Forced motion: flow conditions for the numerical simulations and the experiments.

Case	α_0 (deg)	f (Hz)	C_{ref} (m/s)	κ	Re
Numerical	2	1–1000	5, 10, 15	0.02–100	$0.5–1.5 \times 10^6$
Experimental	2	2, 10, 20	5, 10, 15	0.04–1.25	$0.5–1.5 \times 10^6$

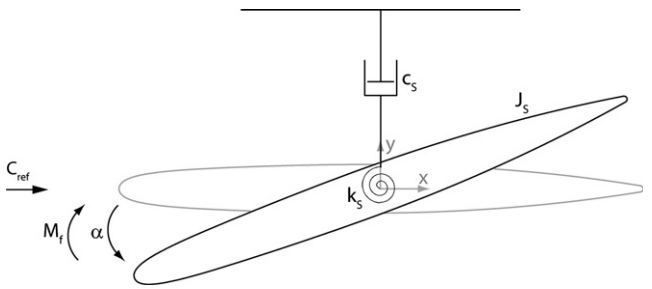

Fig. 3. Sketch of the free oscillating case.

Table 2
Free motion: flow conditions for the numerical simulations.

α_0 (deg)	C_{ref} (m/s)	J_s (kg m^2)	μ_s (kg m^2 s^{-1})	k_s (N m)	Re
2	5	1×10^{-5}	4×10^{-4}–0.12	1, 30	0.5×10^{6}

Table 3
Sensor locations.

Pressure sensor	x/L	y/h	z/B
p1	−0.48	−0.19	0.47
p2	−0.30	−0.43	0.47
p3	−0.10	−0.50	0.47
p4	0.10	−0.47	0.47
p5	0.30	−0.33	0.47
p6	0.40	−0.21	0.47

Table 4
Numerical parameters.

Simulation type	Unsteady
Spatial scheme	2nd order specified blend factor: 1
Temporal scheme	2nd order backward Euler
Time step	$\Delta t = T/480$
Turbulence model	SST
Convergence	Maximum residual of 10^{-4}, 8 coefficient loops per time step

2.2. Experimental procedure

The EPFL High-Speed Cavitation Tunnel is a closed-loop with a test-section measuring $150\times150\times750\,\text{mm}^3$ (Avellan et al., 1987). The experimental 2-D hydrofoil had a span, B, of 150 mm. An oscillating system generated the angular pitching oscillations by differing frequency and amplitude. The driving system is detailed in Caron (2000). The experimental conditions are given in Table 1. Six miniature piezo-resistive pressure transducers were flush mounted along the chord length on one side of the hydrofoil; see Fig. 1 and Table 3. The sensors had a diameter of 3 mm, a height of 1 mm and a pressure measuring range of 0–0.7 MPa and were embedded in previously bored cylindrical cavities. Each cavity was connected to the surface through a small pipe filled with a plastic compound acting also as a protective layer for the sensor, which ensured a good surface finish and enabled the pressure sensors profile to be as thin as 2 mm without altering the hydraulic profile. The data acquisition system had an A/D resolution of 16 bytes, a memory depth of 1 MSamples/channel and maximum sampling frequency of 51.2 kHz/channel. The test-section pressure was held constant at a sufficiently high value to avoid any cavitation development.

2.3. Numerical procedure

The unsteady numerical simulations were performed with the commercial software, ANSYS CFX 11®, based on the finite volume method, the software solves both the incompressible Unsteady Reynolds Averaged Navier–Stokes URANS equations in their conservative form and the mass conservation equation. The set of equations is closed-formed and is solved using a two-equation turbulence model, the shear stress transport (SST) model (Menter, 1994). The SST model uses the $k-\omega$ model (Wilcox, 1993) close to surfaces and the $k-\varepsilon$ model (Launder and Spalding, 1974) far away from the surfaces. The equations were discretized by the backward Euler implicit scheme, second order in time and an advection scheme with a specified blend factor equal to one corresponding to a second order in space. The numerical parameters are summarized in Table 4.

The rectangular computational domain of the 2-D hydrofoil was discretized with a structured mesh, as seen in Fig. 4. The domain had a span of $e = 1$ mm discretized with two nodes. The characteristics of the computational domain are

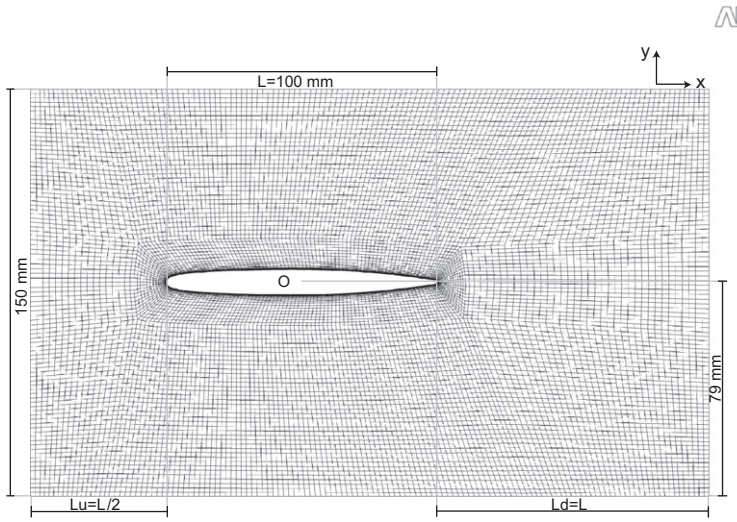

Fig. 4. Computational domain.

Table 5
Characteristics of the computational domain.

Mesh type	Number of nodes	Min face angle	Max y_{plus}
Structured	40 000	38°	5

summarized in Table 5, y_{plus} being the classical non-dimensional distance for wall-bounded flow defined as $y_{plus} = u_\tau y/v$, where u_τ is the friction velocity.

Depending on whether a forced or free motion case was being simulated, the motion of the hydrofoil wall was either specified or calculated. The displacement of the hydrofoil wall boundary was then used to update the inner nodes of the computational domain by solving the diffusion equation using the moving mesh option in ANSYS CFX 11®. The mesh deformation was determined by the mesh stiffness which, in the present study, was specified to be inversely proportional to the wall distance to mitigate the mesh distortion close to the wall region of the hydrofoil. The following are the imposed boundary conditions: no-slip condition at the hydrofoil wall; uniform velocity C_{ref} in the $\vec{x}$ direction fixed at the inlet with a turbulent intensity of 1% and an eddy viscosity ratio of 10; a constant average static pressure imposed at the outlet, which was verified afterwards in the simulation; symmetrical conditions at the side planes in the span-wise direction; symmetrical conditions at the top and bottom walls of the computational domain, as opposed to a solid wall boundary conditions, which would require further mesh refinement. The last boundary condition is reasonable because the blockage ratio, β, defined as the ratio between the maximum thickness of the profile and the height of the tunnel test section, is less than 7% and thus the effect of blockage is negligible (West and Apelt, 1982). The initial condition is a uniform velocity of C_{ref} with a turbulent intensity of 1% and an eddy viscosity ratio of 10.

3. Results

3.1. Experimental validation

The numerical simulations were experimentally validated for the forced motion case. The maximum hydrodynamic torque amplitude, M, was used to test the sensitivities of the meshes and check the time step independency. Each case was performed with a reduced frequency $\kappa = 3.14$. Three meshes of varying boundary layer mesh refinements were tested, as seen in Table 6. The difference between the medium and the fine mesh was smaller than 0.3%. The medium mesh was selected to save computational time with a maximum value for y_{plus} of 5 chosen to be sufficient to capture the

Table 6
Influence of mesh size and computational domain extension for $\kappa = 3.14$.

Case	Coarse	Medium	Fine	Extended
Elements	20 000	40 000	80 000	160 000
Max y_{plus}	50	5	1	5
It. per period	480	480	480	480
Time step (s)	2.1×10^{-5}	2.1×10^{-5}	2.1×10^{-5}	2.1×10^{-5}
M_{max} (N.m)	5.32×10^{-2}	5.38×10^{-2}	5.40×10^{-2}	5.37×10^{-2}
Sensitivity	1.39%	0.27%	0%	0.25%

Table 7
Influence of time step for $\kappa = 3.14$.

Case	Δt_1	Δt_2	Δt_3
Elements	40 000	40 000	40 000
Max y_{plus}	5	5	5
It. per period	120	480	1920
Time step (s)	8.3×10^{-5}	2.1×10^{-5}	0.5×10^{-5}
M_{max} (N m)	5.44×10^{-2}	5.38×10^{-2}	5.37×10^{-2}
Sensitivity	1.27%	0.25%	0%

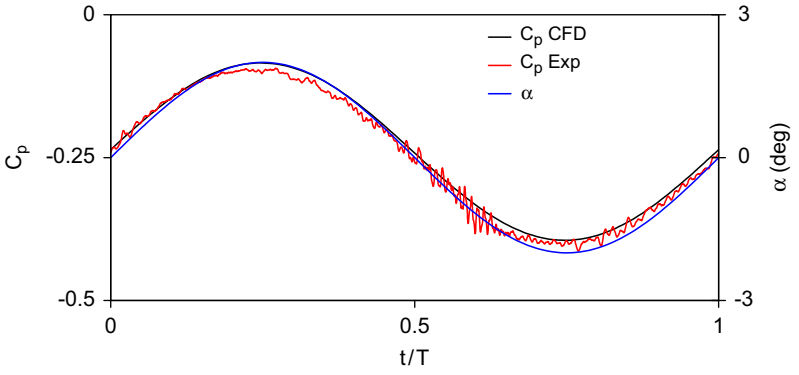

Fig. 5. Time history over 1 period of the incidence angle and the C_p values for pressure sensor p_2, for the numerical simulations and the experiments when $\kappa = 0.21$.

boundary layer phenomena (Menter, 1994). To further test the medium mesh, an extended computational domain of the mesh was created, where the upstream distance to the hydrofoil was $Lu = 5\,L$ and the downstream distance was $Ld = 10\,L$. The difference between the medium mesh and the extended medium mesh was less than 0.3%. The smaller computational domain was thus selected.

Finally, three time steps were tested (120, 480 and 1920 iterations per period), as seen in Table 7. The hydrodynamic torque amplitude with 480 iterations per period (Δt_2) was only 0.25% higher than with using the smaller time step. Therefore computations were made with 480 iterations per period.

The numerical simulation was verified by comparing the time history of the pressure coefficient, C_p, over 1 period with the experimental results, as seen in Fig. 5, where

$$C_p = \frac{p - p_{inlet}}{\frac{1}{2}\rho C_{ref}^2}. \tag{5}$$

By integrating the computed pressure values at the hydrofoil wall over 1 period, the hydrodynamic torque was obtained and compared with the measured values, thereby further validating the numerical simulation, as seen in Fig. 6

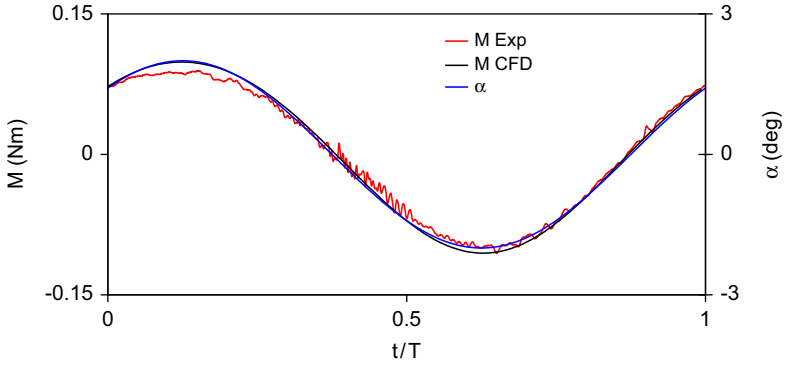

Fig. 6. Time history over 1 period of the incidence angle and the hydrodynamic torque for the numerical simulations and the experiments when $\kappa = 0.21$.

and the equation below

$$M = \sum_{i=1}^{6} \left(p(M_i, t) + p\left(M_i, t + \frac{\tau}{2}\right) \right) \overrightarrow{\delta A}(M_i) \wedge \overrightarrow{OM_i}, \tag{6}$$

where p is the wall pressure, M_i is the sensor location, O is the center of gravity, $\delta \overrightarrow{A}(M_i)$ is the surface element centered at the sensor location and τ is the period of motion. The symmetry and periodicity properties of the case study were taken into account, and the friction contribution was neglected. The good agreement between the numerical and experimental results shows that the numerical simulations can accurately predict the pressure and thus, predict the pressure contribution to the hydrodynamic torque.

3.2. Hydrodynamic load analysis

The model of the hydrodynamic torque was developed from the numerical model by assuming the flow response of the hydrofoil motion is a linear combination of the angular position and its derivatives. This assumption is a classical approach to model linear, unsteady aerodynamic applications with a small angle of attack. Therefore, the inertia, damping and stiffness coefficients are as follows:

$$M = -(J_f \ddot{\alpha} + \mu_f \dot{\alpha} + k_f \alpha). \tag{7}$$

A sinusoidal forced motion was used to investigate the added moment of inertia J_f, the fluid damping μ_f and the fluid stiffness k_f. Let $\mathcal{A}(f)$ be the Fourier transform of the sinusoidal forced incidence, $\alpha(t)$, and $\mathcal{M}(f)$ be the Fourier transform of the resulting torque, $M(t)$. By taking the Fourier transform of Eq. (7), the following result is obtained:

$$\mathcal{M}(f) = -(-(2\pi f)^2 J_f + i(2\pi f)\mu_f + k_f)\mathcal{A}(f). \tag{8}$$

Let the complex transfer function, $H(f)$ be the transfer function defined by

$$\mathcal{A}(f) = H(f)\mathcal{M}(f). \tag{9}$$

Then, by replacing $2\pi f$ with ω, the transfer function is obtained as

$$H(\omega) = \frac{1}{J_f \omega^2 - k_f - \mathrm{i}\mu_f \omega}. \tag{10}$$

The magnitude of the transfer function, $|H(\omega)|$, and the phase, $\phi(\omega)$, were both investigated in the frequency domain. The ratio of the magnitudes, the phase differences of the sinusoidal forced incidence and the resulting torque were calculated to identify the model parameters:

$$|H(\omega)| = \frac{|\mathcal{A}(\omega)|}{|\mathcal{M}(\omega)|} = \frac{1}{\sqrt{(J_f \omega^2 - k_f)^2 + (\mu_f \omega)^2}}, \tag{11}$$

$$\phi(\omega) = \arg(\mathcal{A}) - \arg(\mathcal{M}) = \arctan\left(\frac{\mu_f \omega}{J_f \omega^2 - k_f}\right). \tag{12}$$

Three values of upstream velocities were considered with oscillation frequencies ranging between 1 and 1000 Hz, as seen in Table 1. The Bode diagram of the magnitude is shown in Figs. 7 and 8. The normalized transfer function, $|H^*(\omega)|$, is defined by

$$|H^*(\omega)| = \frac{|H(\omega)|}{|H(0)|}, \tag{13}$$

where $|H(0)|$ corresponds to the steady case at a 0° incidence.

As proposed in the model, the shape of the transfer function corresponds to a second-order law. At low frequencies, $|H|$ tends to a constant value corresponding to static motion. When normalized, $|H^*|$ becomes independent of the upstream velocity, as seen in Fig. 8. At high frequencies, the transfer function displays an asymptotic behavior. Assuming that the stiffness and the damping terms are negligible at high frequencies, the asymptotic behavior is then identified by

$$|H(\omega)| \sim \frac{1}{J_f \omega^2} \quad \text{for } \omega \to \infty. \tag{14}$$

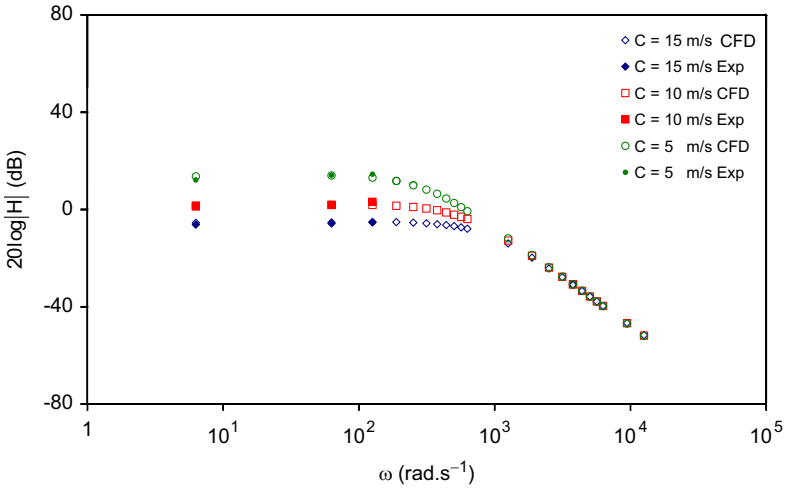

Fig. 7. Bode diagram of the magnitude $|H|$ as a function of ω: numerical and experimental results.

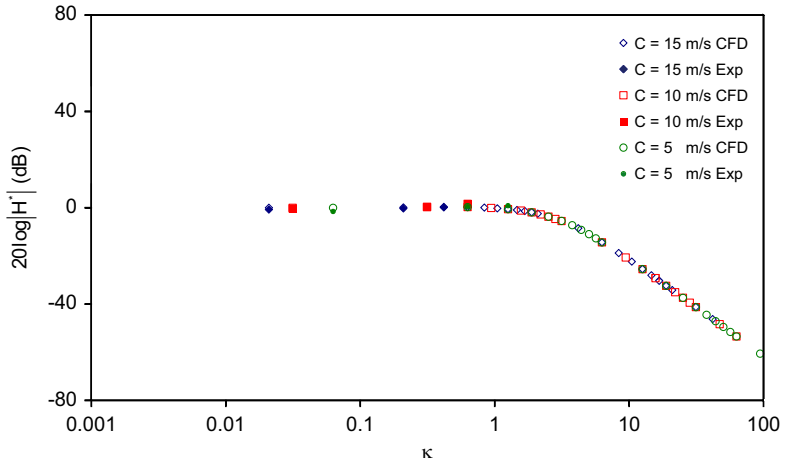

Fig. 8. Bode diagram of the dimensionless value $|H^*|$ as a function of κ: numerical and experimental results.

The above assumption is confirmed later in the paper. The phase shift between the forced motion and the fluid response is plotted in Fig. 9 as a function of reduced frequency for three values of the upstream velocity. The phase shift is found to be independent of the upstream velocity in this range of Reynolds numbers. A maximum value of 20° is reached when $\kappa \simeq 1$, which corresponds to a transit-time and motion period of the same order. When $\kappa 1$ and $\kappa \gg 1$, the hydrofoil motion and the torque are in phase, and the phase shift tends to the constant value of 0°.

The added moment of inertia, the fluid damping and fluid stiffness coefficients can now be identified. The moment of inertia, J_f, is identified with the asymptotic matching of the magnitude when $\kappa \gg 1$ using Eq. (14) and assuming that J_f does not depend on the motion frequency, which will be confirmed later in the paper. The estimated moment of inertias for the three values of C_{ref} are given in Table 8. Additionally, the corresponding potential value is given in Table 8. According to Brennen (1982), the theoretical value of the added moment of inertia for a thin plate in rotation around its center of mass is defined by

$$J = \frac{1}{8}\rho\pi\left(\frac{L}{2}\right)^4 b, \tag{15}$$

where b is the span and L is the chord length. The added moment of inertia as calculated with Eq. (15) is equal to the constant value computed in the three numerical simulations, as seen in Table 8, which validates the assumption that J_f does not depend on the upstream velocity or the motion frequency. Therefore, an added moment of inertia of $2.45 \times 10^{-6}\,\text{kg m}^2$ is assumed in the following sections.

The fluid stiffness coefficient, k_f, is then identified through the real part of the transfer function:

$$\begin{aligned} &\text{Re}(H) = |H|\cos(\phi), \\ &\text{Re}(H) = |H|^2(J_f\omega^2 - k_f), \\ &k_f = J_f\omega^2 - \frac{\cos(\phi)}{|H|}. \end{aligned} \tag{16}$$

The dimensionless stiffness coefficient k^* is then defined as

$$k^* = \frac{k_f}{\frac{1}{2}\rho C_{\text{ref}}^2 AL}, \tag{17}$$

where $A = L \times e$ is the cross-section area. In Fig. 10, k^* is plotted as a function of κ for three values of the upstream velocity with corresponding fitted linear laws. Low frequencies are shown with more detail is provided in Fig. 11.

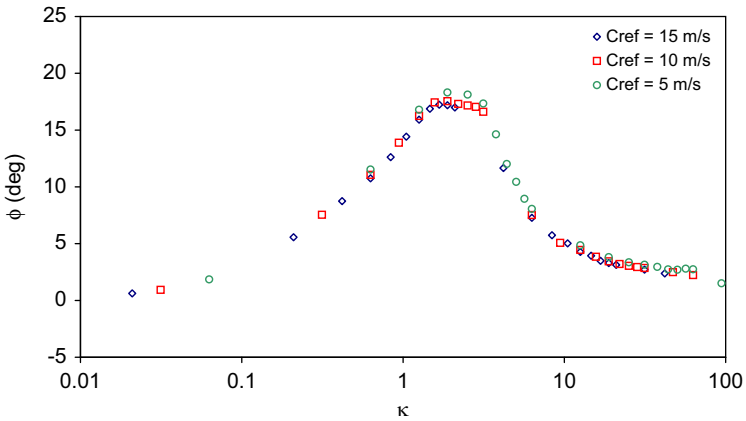

Fig. 9. Bode diagram of the phase as a function of κ: numerical results.

Table 8
Added moment of inertia.

C_{ref} (m/s)	5	10	15	Potential flow
J_f (kg m^2)	2.46×10^{-6}	2.45×10^{-6}	2.45×10^{-6}	2.45×10^{-6}

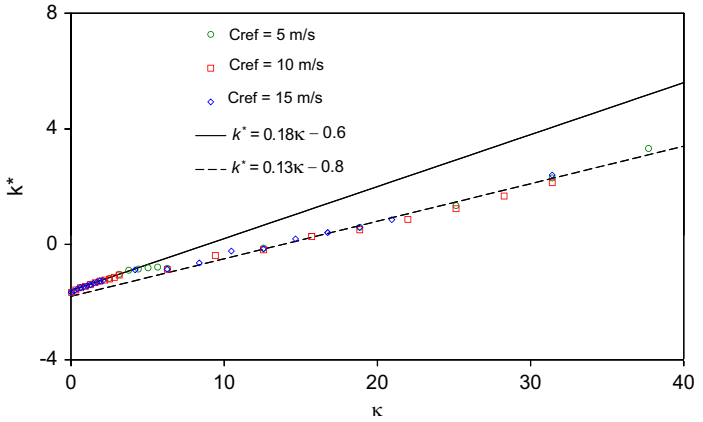

Fig. 10. Dimensionless fluid stiffness coefficient for the entire reduced frequency range.

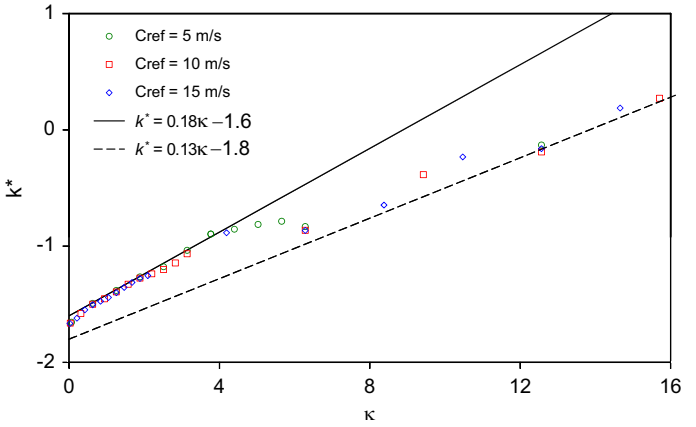

Fig. 11. Dimensionless fluid stiffness coefficient for lower values of the reduced frequency.

According to the above result, k^* is found to be independent of the upstream velocity but dependent on the reduced frequency.

When $\kappa \leq 14$, the dimensionless fluid stiffness coefficient is negative; for such cases, the fluid stiffness acts in a way that moves the profile away from the reference position, $\alpha = 0^\circ$. When $\kappa \leq 4$ and $\kappa \geq 12$, two linear behavioral laws are found:

$$k^* = 0.18\kappa - 1.6 \quad \text{for } \kappa \leq 4; \tag{18}$$

$$k^* = 0.13\kappa - 1.8 \quad \text{for } \kappa \geq 12. \tag{19}$$

In-between these limits, transitional behavior occurs. The origin of this transition will be discussed later in the paper. As assumed in Eq. (14), the stiffness term is found to be negligible at high frequencies:

$$\frac{k_f(\omega)}{J_f\omega^2} \approx 10^{-3} \ll 1 \quad \text{for } \omega \to \infty. \tag{20}$$

The fluid damping coefficient is then found through the imaginary part of the transfer function:

$$\begin{aligned} &Im(H) = |H|\sin(\phi), \\ &Im(H) = |H|^2 \mu_f \omega, \\ &\mu_f = \frac{\sin(\phi)}{|H\omega|}. \end{aligned} \tag{21}$$

As for the fluid stiffness, the fluid damping can be scaled as follows:

$$\mu^* = \frac{\mu_f}{\frac{1}{4}\rho C_{\text{ref}} A L^2}. \tag{22}$$

In Fig. 12, μ^* is plotted as a function of the reduced frequency κ for three values of the upstream velocity. The low values of κ are emphasized in Fig. 13.

As with k^*, μ^* is independent of the upstream velocity but varies with κ and is always positive. When $\kappa \leq 4$ and $\kappa \geq 12$, two behavioral power laws are found:

$$\mu^* = 0.42\kappa^{-0.4} \quad \text{for } \kappa \leq 4; \tag{23}$$

$$\mu^* = 0.04\kappa^{0.6} \quad \text{for } \kappa \geq 12. \tag{24}$$

In-between these limits, as observed for k^*, a transitional behavior is observed when $4 \leq \kappa \leq 12$. As assumed in Eq. (14), the damping term is found to be negligible at high frequencies:

$$\frac{\mu_f(\omega)}{J_f \omega} \approx 10^{-2} \ll 1 \quad \text{for } \omega \to \infty. \tag{25}$$

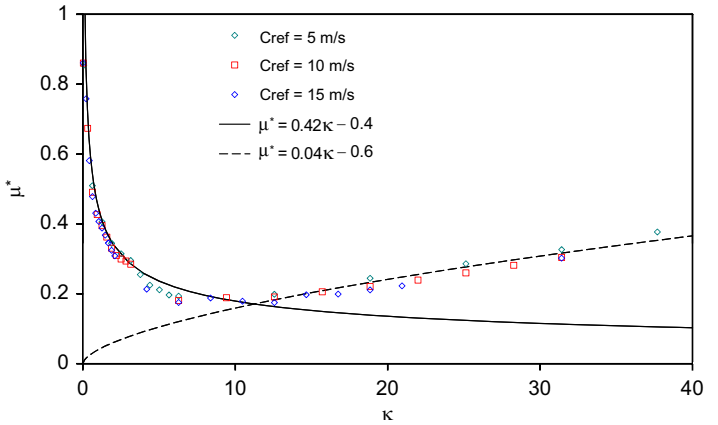

Fig. 12. Dimensionless fluid damping coefficient for the entire reduced frequency range.

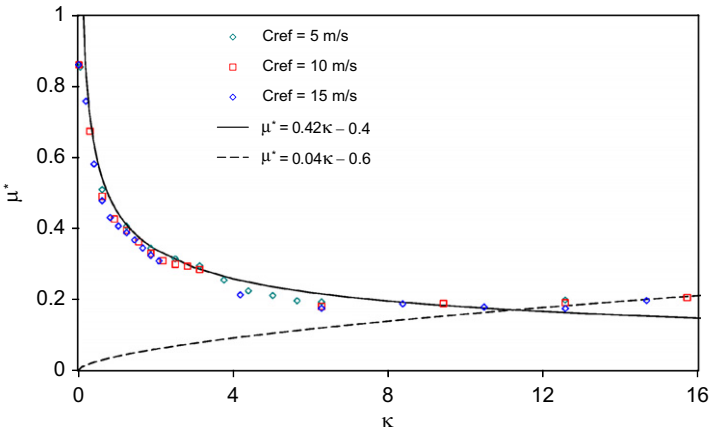

Fig. 13. Dimensionless fluid damping coefficient for lower values of the reduced frequency.

The origin of the transition observed for k^* and μ^* when $4 \leq \kappa \leq 12$ is investigated by considering the scaled vorticity defined as

$$\Omega_n = \left(\frac{\partial C_y}{\partial x} - \frac{\partial C_x}{\partial y}\right)\frac{L}{C_{\text{ref}}}. \tag{26}$$

The vorticity, Ω_n, is plotted in Fig. 14 when $C_{\text{ref}} = 15\,\text{m/s}$ for four values of the reduced frequency.

According to the four pictures in Fig. 14, the flow dynamic in the wake starts to change dramatically when the reduced frequency is equal to 4. The two layers of vorticity undulate with a decreasing wake length and cross-section when $\kappa \approx 4.6$, and at higher reduced frequencies, vortices develop, as seen in Fig. 14(d), which can lead to thrust development (Koochesfahani, 1989; Triantafyllou et al., 1993). The development of the vortices influences the hydrodynamic torque, which explains the behavioral modification observed when k^* and μ^* for $4 \leq \kappa \leq 12$.

3.3. Model assessment

In this section, the model of the hydrodynamic torque is applied to the free motion case, again assuming a linear flow response of the hydrofoil motion as defined in Eq. (7). The hydrofoil is attached to a flexible structure, described in Section 2.1. In the model, the hydrofoil initially departs from rest (no initial velocity) from an incidence angle of 2° and then freely oscillates. Six cases were investigated, where structural damping and stiffness coefficients were varied, as seen in Table 9. Additionally, two reduced frequencies were used where vortices either did or did not develop, respectively, for cases 1 and 2. For each type of flow, solutions for an under damped, critically damped and over damped conditions were solved with the model.

The free oscillating system is given as

$$M = J_s\ddot{\alpha} + \mu_s\dot{\alpha} + k_s\alpha. \tag{27}$$

Using the linearized model of the hydrodynamic torque, Eq. (27) can be rewritten as

$$(J_s + J_f)\ddot{\alpha} + (\mu_s + \mu_f)\dot{\alpha} + (k_s + k_f)\alpha = 0, \tag{28}$$

$$\ddot{\alpha} + 2\xi\omega_0\dot{\alpha} + \omega_0^2\alpha = 0, \tag{29}$$

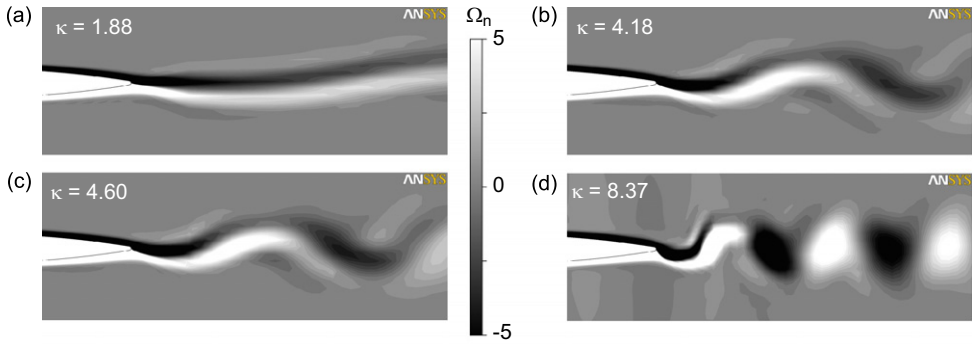

Fig. 14. Cross sections of the scaled vorticity for four values of κ.

Table 9
Operating conditions for the assessment.

	κ	C_{ref} (m/s)	J_s (kg m^2)	k_s (Nm)	μ_s (kg m^2 s^{-1})
Case 1*a*	2.62	5	1×10^{-5}	1	4×10^{-4}
Case 1*b*	2.62	5	1×10^{-5}	1	6.2×10^{-3}
Case 1*c*	2.62	5	1×10^{-5}	1	2×10^{-2}
Case 2*a*	15.50	5	1×10^{-5}	30	5×10^{-3}
Case 2*b*	15.50	5	1×10^{-5}	30	3.9×10^{-2}
Case 2*c*	15.50	5	1×10^{-5}	30	1.2×10^{-1}

with the motion pulsation, ω_0, and the damping ratio, ξ, by

$$\omega_0 = \sqrt{\frac{k_s + k_f}{J_s + J_f}}, \tag{30}$$

$$\xi = \frac{\mu_s + \mu_f}{\mu_c}, \tag{31}$$

where the critical damping, μ_c, is defined by

$$\mu_c = 2\sqrt{(J_s + J_f) \times (k_s + k_f)}. \tag{32}$$

The analytical solution depends on the damping ratio, and thus, there are three possible solutions as follows:
The underdamped case: $\xi < 1$

$$\alpha = \alpha_0 e^{-\xi\omega_0 t}\left(\cos(\omega_0\sqrt{1-\xi^2}t) + \frac{\xi}{\sqrt{1-\xi^2}}\sin(\omega_0\sqrt{1-\xi^2}\,t)\right). \tag{33}$$

The critically damped case: $\xi = 1$

$$\alpha = \alpha_0 e^{-\omega_0 t}(1 + \omega_0 t). \tag{34}$$

The overdamped case: $\xi > 1$

$$\alpha = \alpha_0 e^{-\xi\omega_0 t}\left(\cosh(\omega_0\sqrt{\xi^2-1}t) + \frac{\xi}{\sqrt{\xi^2-1}}\sinh(\omega_0\sqrt{\xi^2-1}\,t)\right). \tag{35}$$

The model was assessed by comparing the incidence angle time history determined by the linearized model of Eqs. (33) and (34) or (35) with the previous coupled fluid–structure simulations as described in Section 2.1.

To calculate $\alpha(t)$ with Eqs. (33) and (34) or (35), ξ and ω_0 must first be evaluated; the fluid coefficients J_f, μ_f and k_f were determined in the same way as in the forced motion case, described in the previous section. The added moment of inertia is constant ($J_f = 2.45 \times 10^{-6}$ kg m^2), as seen in Table 5. The fluid stiffness and damping coefficients were calculated with Eqs. (18) and (23) in cases 1 ($\kappa \leq 4$) and with Eqs. (19) and (24) in cases 2 ($\kappa \geq 12$). The coefficients are presented in Table 10. The motion pulsation and the damping ratio, ω_0^m and ξ^m, were then calculated for each case with Eqs. (30) and (31).

The incidence angle from the coupled fluid–structure simulation of the free motion is fitted with this analytical solution to extract ξ^s and ω_0^s. In Table 11, ξ^m and ω_0^m, the damping ratio and motion pulsation from the model, and ξ^s and ω_0^s extracted from the coupled fluid–structure simulations are given for the different cases. The relative differences between the model and the simulation are shown and reveal excellent agreement.

Fig. 15 shows the modeled and simulated time histories of the incidence angle plotted for the six cases. There is excellent agreement between the coupled fluid–structure simulation, and the model is confirmed. Thus, it has been shown that the forced motion simulation is sufficient to predict the fluid–structure coupling of the free motion case and avoid coupled fluid–structure simulations, thereby saving a significant amount of time. This method was successfully validated for a small motion amplitude with linear assumption for a maximum value of $\alpha_0 = 5^\circ$.

To identify all model parameters, eight numerical simulations (eight different reduced frequencies) must be performed for the forced motion case. The corresponding required computational time was 2 h per simulation with 4 cores Intel Xeon Nehalem, 2.93 GHz. Therefore, the total CPU time to entirely define the hydro-elastic behavior of the oscillating hydrofoil is 16 h. For every single coupled fluid–structure simulation for the free motion case, a computational time of 4 h per simulation is required using the same computational system.

Table 10
Assessment: added moment of inertia, fluid stiffness and damping coefficient.

	κ	J_f (kg m^2)	k_f (Nm)	μ_f (kg m^2 s^{-1})
Cases 1	2.62	2.45×10^{-6}	−0.14	3.82×10^{-4}
Cases 2	15.50	2.45×10^{-6}	0.026	2.59×10^{-4}

Table 11
Assessment: damping ratio and motion pulsation.

	ξ^m	ξ^s	$\frac{\lvert\xi^m-\xi^s\rvert}{\xi^s}$ (%)	ω_0^m (rad/s)	ω_0^s (rad/s)	$\frac{\lvert\omega_0^m-\omega_0^s\rvert}{\omega_0^s}$ (%)
Case 1*a*	1.20×10^{-1}	1.20×10^{-1}	0.7	263	264	0.4
Case 1*b*	1	1.02	2	263	258	1.1
Case 1*c*	3.11	3.16	1.2	263	264	0.4
Case 2*a*	1.36×10^{-1}	1.38×10^{-1}	1.4	1553	1560	0.4
Case 2*b*	1	1.01	1	1553	1558	0.3
Case 2*c*	3.11	3.12	0.3	1553	1560	0.4

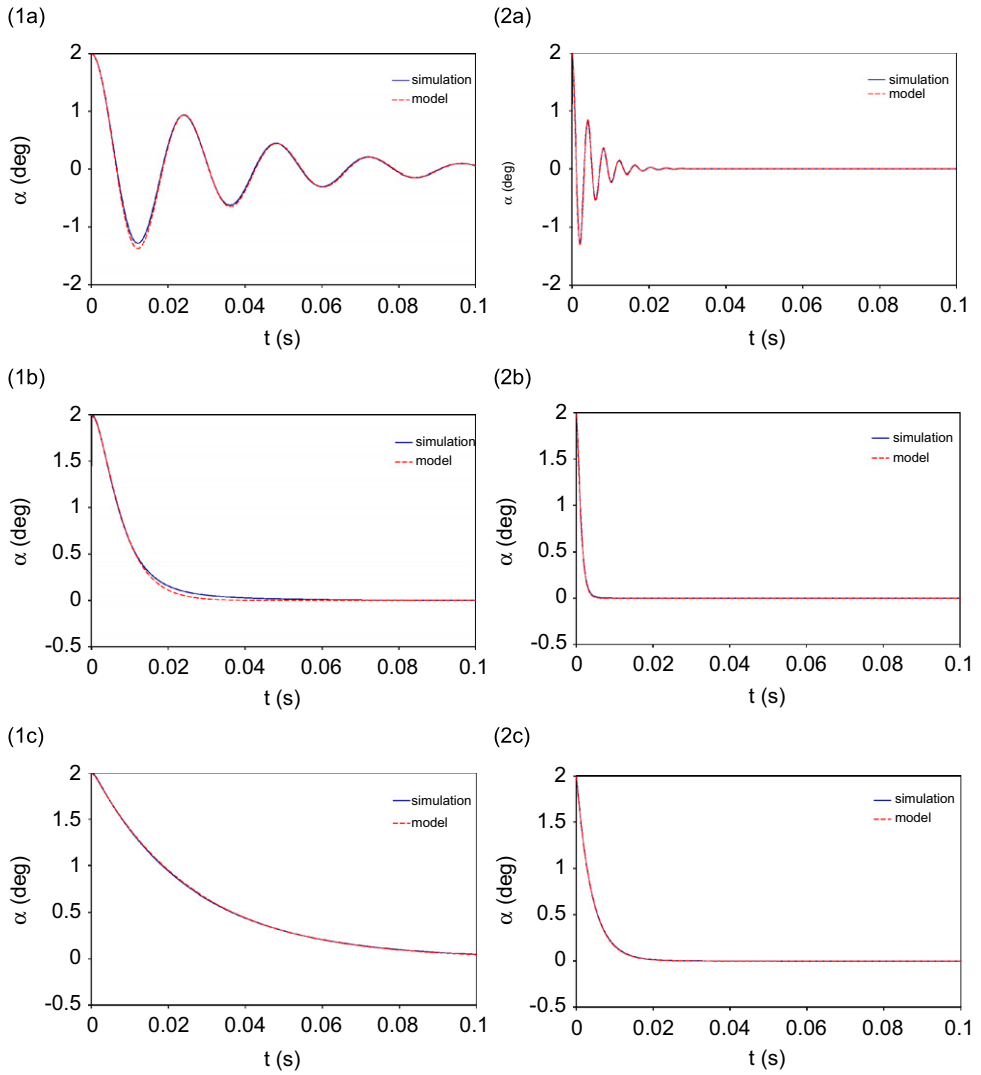

Fig. 15. Time history of the incidence angle: model and coupled fluid–structure simulation in cases 1 and 2 (a), (b) and (c).

4. Conclusion

In this paper, a model is proposed that predicts fluid–structure coupling by linearizing the hydrodynamic load acting on a rigid, oscillating hydrofoil (NACA 0009) surrounded by an incompressible, turbulent flow. Forced and free

pitching motions were both investigated with a mean incidence angle of 0° and a maximum angle amplitude of 2°. The unsteady simulations of the flow were performed in ANSYS CFX and validated experimentally. An analysis of the hydrodynamic load was performed as a function of the reduced frequency, varying from 0.02 to 100, and the Reynolds number, varying from 5×10^5 to 1.5×10^6. The hydrodynamic load was linearized by combining the added moment of inertia, fluid damping and fluid stiffness effects. The added moment of inertia was found to be constant as expected from the potential flow analysis. With respect to the fluid damping and the fluid stiffness coefficients, new results were found. Both coefficients can be expressed as a function of the reduced frequency with an appropriate normalization. When $\kappa \leq 4$ and $\kappa \geq 12$, quadratic and power laws were found, respectively, for k^*, the dimensionless fluid stiffness coefficient and μ^*, the dimensionless fluid damping coefficient. In between the two limits, a perturbation arises, and the flow dynamic in the wake of the hydrofoil is changed when $\kappa \simeq 4.6$. The two layers of vorticity found in the wake, combine to form a discrete concentration of vorticity. Those vortices can lead to thrust generation, and the drag and the hydrodynamic torque are modified. For a given value of the reduced frequency, the presented model can predict the hydrodynamic torque on the hydrofoil.

To validate the method, a simulation was performed with the hydrofoil attached to a flexible structure. Six cases were investigated, that varied the value of the structural damping and stiffness coefficients. Two values of the reduced frequency were investigated to study cases with and without vortices in the wake. The time history of the incidence angle was used for the validation. The incidence angle, $\alpha(t)$, was first determined using the linearized model with the expected analytical solution and then simulated as a coupled fluid–structure simulation in ANSYS CFX. An excellent agreement was found, the differences in damping ratio and motion pulsation in the six cases were less than 2%. In conclusion, the results show that the proposed model can predict fluid–structure coupling with good precision when the response of the system is linearized. The method was successfully validated for a maximum value of 5° for the motion amplitude.

Acknowledgements

The investigation reported in this paper is part of the work carried out for the HYDRODYNA, Eureka Research Project n 3246, whose partners are the following: ALSTOM Hydro, ANDRITZ Hydro, EPFL, VOITH Hydro and UPC CDIF. The project is also financially supported by the Swiss Federal Commission for Technology and Innovation (CTI) and Swisselectric Research. The authors are very grateful to the HYDRODYNA technical committee for its involvement and constant support in the project. Finally the staff of the Laboratory for Hydraulic Machines should be thanked for their support in the experimental and numerical work.

References

Abbott, I.H, Von Doenhoff, A.E., Albert, E., 1945. Summary of airfoil data. NACA Report, 824.

Ausoni, P., Farhat, M., Escaler, E., Egusquiza, E., Avellan, F., 2007. Cavitation influence on von karman vortex shedding and induced hydrofoil vibrations. ASME Journal of Fluids Engineering 129, 966–973.

Avellan, F., Henry, P., Ryhming, I.L., 1987. A new high speed cavitation tunnel. ASME Winter Annual Meeting, Boston 57, 49–60.

Brennen, C.E., 1982. A review of added mass and fluid inertial forces, Naval Civil Engineering Laboratory.

Caron, J.F., 2000. Etude de l'influence des instationnarités des écoulements sur le développement de la cavitation. Thèse EPFL 2284.

Carstens, V., Kemme, R., Schmitt, S., 2003. Coupled simulation of flow-structure interaction in turbomachinery. Aerospace Science and Technology 7, 298–306.

Conca, C., Osses, A., Planchard, J., 1997. Added mass and damping in fluid–structure interaction. Computer Methods in Applied Mechanics and Engineering 146, 387–405.

Dowell, E.H., Hall, K.C., 2001. Modeling of fluid–structure interaction. Annual Review of Fluid Mechanics 33, 445–490.

Ducoin, A., Astofli, J.A., Deniset, F., Sigrist, J.F., 2009. An experimental and numerical study of the hydroelastic behavior of an hydrofoil in transient pitching motion. In: First International Symposium on Marine Propulsors, Trondheim, Norway.

Gnesin, V.I., Kolodyazhnaya, L.V., Rzadkowski, R., 2004. A numerical modelling of stator–rotor interaction in a turbine stage with oscillating blades. Journal of Fluids and Structures 19, 1141–1153.

Koochesfahani, M.M., 1989. Vortical patterns in the wake of an oscillating airfoil. AIAA Journal 27, 1200–1205.

Launder, B.E., Spalding, D.B., 1974. The numerical computation of turbulent flows. Computer Methods in Applied Mechanics and Engineering 3 (2), 269–289.

Marshall, J.G., Imregun, M., 1996. A review of aeroelasticity methods with emphasis on turbomachinery applications. Journal of Fluids and Structures 11, 973–982.

Menter, F.R., 1994. Two-equation eddy-viscosity turbulence models for engineering application. AIAA Journal 32 (8), 1598–1605.

Moffatt, S., He, L., 2005. On decoupled and fully-coupled methods for blade forced response prediction. Journal of Fluids and Structures 20, 217–234.

Nicolet, C., Ruchonnet, N., Avellan, F., 2006. One-dimensional modeling of rotor stator interaction in Francis pumpturbine. In: 23rd IAHR Symposium, Yokohama.

Triantafyllou, G.S., Triantafyllou, M.S., Grosenbaugh, M.A., 1993. Optimal thrust development in oscillating foils with application to fish propulsion. Journal of Fluids and Structures 7, 205–224.

Wang, W.Q., He, X.Q., Zhang, L.X., Liew, K.M., Guo, Y., 2009. Strongly coupled simulation of fluid–structure interaction in a francis hydroturbine. International Journal for Numerical Methods in Fluids 60, 515–538.

West, G.S., Apelt, C.J., 1982. The effects of tunnel blockage and aspect ratio on the mean flow past a circular cylinder with Reynolds numbers between 10^4 and 10^5. Journal of Fluid Mechanics 114, 301–377.

Wilcox, D., 1993. Comparison of two-equation turbulence models for boundary layers with pressure gradient. AIAA Journal 31 (8), 1414–1421.

Young, Y.L., 2007. Time-dependant hydroelastic analysis of cavitating propulsors. Journal of Fluids and Structures 23, 269–295.

Young, Y.L., 2008. Fluid–structure interaction analysis of flexible composite marine propellers. Journal of Fluids and Structures 24, 799–818.

Zobeiri, A., Kueny, J.L., Fahrat, M., Avellan, F., 2006. Pump-turbine rotor–stator interactions in generating mode: pressure fluctuation in distributor channel. In: 23rd IAHR Symposium, Yokohama, Japan.